Highly Efficient Circularly Polarized Near-infrared Phosphorescence in Both Solution and Aggregate

Dan Liu[†1], Wenjin Wang[†1], Parvej Alam[1], Zhan Yang[1], Kaiwen Wu[1], Lixun Zhu[1], Yu Xiong[3], Shuai Chang[4], Yong Liu[5], Bo Wu[1], Qian Wu[2], Zijie Qiu*[1], Zheng Zhao*[1], Ben Zhong Tang*[1,2,]

[1] Clinical Translational Research Center of Aggregation-Induced Emission, School of Medicine, The Second Affiliated Hospital, School of Science and Engineering, Shenzhen Institute of Aggregate Science and Technology, The Chinese University of Hong Kong, Shenzhen (CUHK-Shenzhen), Guangdong 518172, P.R. China
[2] Department of Chemistry, Hong Kong Branch of Chinese National Engineering Research Center for Tissue Restoration and Reconstruction, Institute of Molecular Functional Materials, Division of Life Science and State Key Laboratory of Molecular Neuroscience, The Hong Kong University of Science and Technology, Clear Water Bay, Kowloon, Hong Kong, China
[3] Center for AIE Research, Shenzhen Key Laboratory of Polymer Science and Technology Guangdong Research Center for Interfacial Engineering of Functional Materials College of Materials Science and Engineering College of Physics and Optoelectronic Engineering, Shenzhen University, Guangdong, 518060, China
[4] Platform for Applied Nanophotonics, Faculty of Materials Science, Shenzhen MSU-BIT University, Shenzhen, 518115, China
[5] Yong Liu, AIE Institute, Guangzhou 510530, China.
[†] These authors contributed equally to this work.
* Email: zijieqiu@cuhk.edu.cn (Z. Q.); zhaozheng@cuhk.edu.cn (Z. Z.); tangbenz@cuhk.edu.cn (B. Z. T.)

Abstract

Circularly polarized phosphorescence (CPP) is a spin-forbidden radiative process with chiroptical activity. The CPP mechanism is far from comprehensively understood, mainly due to the limited examples of efficient triplet emission from small chiral organic molecules with well-defined structures. Herein, a pair of chiral enantiomers *R*/*S*-**BBTI** is reported, featuring the highly distorted spiral ring-locked heteroaromatics with heavy iodine atoms. These chiral molecules emit NIR phosphorescence and exhibit considerable high dissymmetry factors up to 0.013 with an efficiency of 4.2% and a lifetime of 119 μs in dimethyl sulfoxide (DMSO) solution after ultraviolet irradiation. Their crystals show efficient CPP with 7.0% quantum efficiency and a lifetime of 166 μs. Extensive experimental chiroptical investigations combined with theoretical calculations reveal an efficient spin-flip process that modulates the electron and magnetic transition dipole moments to enhance CPP performance. Moreover, the phosphorescence of *R*/*S*-**BBTI** is oxygen-sensitive and photoactivated in DMSO. Therefore, *R*/*S*-**BBTI** can be applied for hypoxia imaging in cells and tumors, expanding the scope of CPP applications.

Main

The efficient generation, manipulation, and controllable emission of triplet excitons in organic materials has enabled significant advances in room-temperature phosphorescence (RTP) research.[1, 2, 3] Despite the formidable challenges posed by triplet emission due to the spin-forbidden transition, rapid advances in material design strategies have facilitated substantial RTP developments.[4, 5] Materials featuring large Stokes shift, long lifetime, and oxygen sensitivity demonstrate promising RTP applications across diverse fields including smart sensors, organic optoelectronic devices, and data storage.[6, 7, 8] While remarkable advances have been made in developing organic RTP materials exhibiting high efficiency and color tunability, achieving efficient near-infrared (NIR) phosphorescence remains a significant challenge. Strategies to lower the triplet state energy often led to increased nonradiative decay and reduced quantum yields.[9] Rationally engineering the excited state dynamics to enable NIR triplet emission while mitigating nonradiative decay is an outstanding challenge.

By introducing chirality into RTP materials, circularly polarized phosphorescence (CPP) with imbalanced left and right circularly polarized light can be expected, unlocking exciting opportunities for cutting-edge applications such as enantioselective sensing, advanced security encryption, 3D displays, high-contrast bioimaging, and energy-saving optoelectronic devices.[10, 11, 12, 13] However, constructing CPP materials is non-trivial, requiring delicate control of high phosphorescence efficiency (Φ_p), long lifetimes (τ_p), and large dissymmetry factors (g_{phos}). Restriction of intra/intermolecular motion (RIM) is the structural description for suppressing the non-radiative decay process and one of the design principles to achieve efficient CPP in crystals, doped matrixes, or polymers.[14, 15, 16] The RIM strategy can tune the key parameters of Φ_p, τ_p, and g_{phos}, but the phosphorescence is sometimes lost in nanoparticles or dilute solutions.[17, 18, 19] Consequently, it is more desirable to maintain CPP in both solution and aggregate states to elucidate the intrinsic structure-property relationship and meet the requirements in different application scenarios.

The early studies on the traditional aromatic compounds in optoelectronic applications have validated the enhanced luminescence resulting from ring-locked engineering.[20, 21, 22] Incorporating chiral elements through asymmetric ring-locking provides control over the three-dimensional geometry and restriction of rotational freedom in the molecular state, while imparting unique chiroptical properties.[23, 24, 25] For example, Zheng et al reported that TPE tetracycle could emit strong fluorescent light in solution due to rotation fixation of the phenyl rings, and stable helical chirality of the propeller-like structure of TPE tetracycle was also obtained.[26] Therefore, ring-locking engineering is a potential strategy to develop state-independent CPP. High-performance NIR-CPP materials can be envisioned when combining ring-locking engineering with other strategies to accelerate intersystem crossing (ISC), such as charge transfer (CT) character, heavy-atom effect, and lone-pair electron incorporation.[27, 28, 29]

In this work, we synthesize two new classes of axially chiral benzothiadiazole derivatives, *R*/*S*-**BBT** and iodine-substituted *R*/*S*-**BBTI**, to investigate the mechanisms governing NIR-CPP. The binaphthol moiety introduces axial chirality and donor-acceptor characteristics, which contribute to circularly polarized luminescence (CPL) and a shift in emission towards the NIR. Additionally, the iodine substituents in *R*/*S*-**BBTI** further boosted the ISC due to the heavy-atom effect (Figure 1). As a result, *R*/*S*-**BBTI** exhibited efficient NIR-CPP in both solution and aggregate states with an efficiency of up to 7.0%. Notably, the fast ISC followed by the spin-flip process changed the orientation and magnitude of transition dipole moments, resulting in chiral inversion and amplification of the dissymmetry factor. Furthermore, tumor hypoxia imaging studies demonstrate the sensitivity of *R*/*S*-**BBTI** as an *in vivo* CPL probe. This integrated synthetic, spectroscopic, and computational approach elucidates structure-property principles to unlock robust and optimized state-independent CPP, providing new opportunities for rationally tailoring triplet excited states toward next-generation chiral phosphorescent technologies.

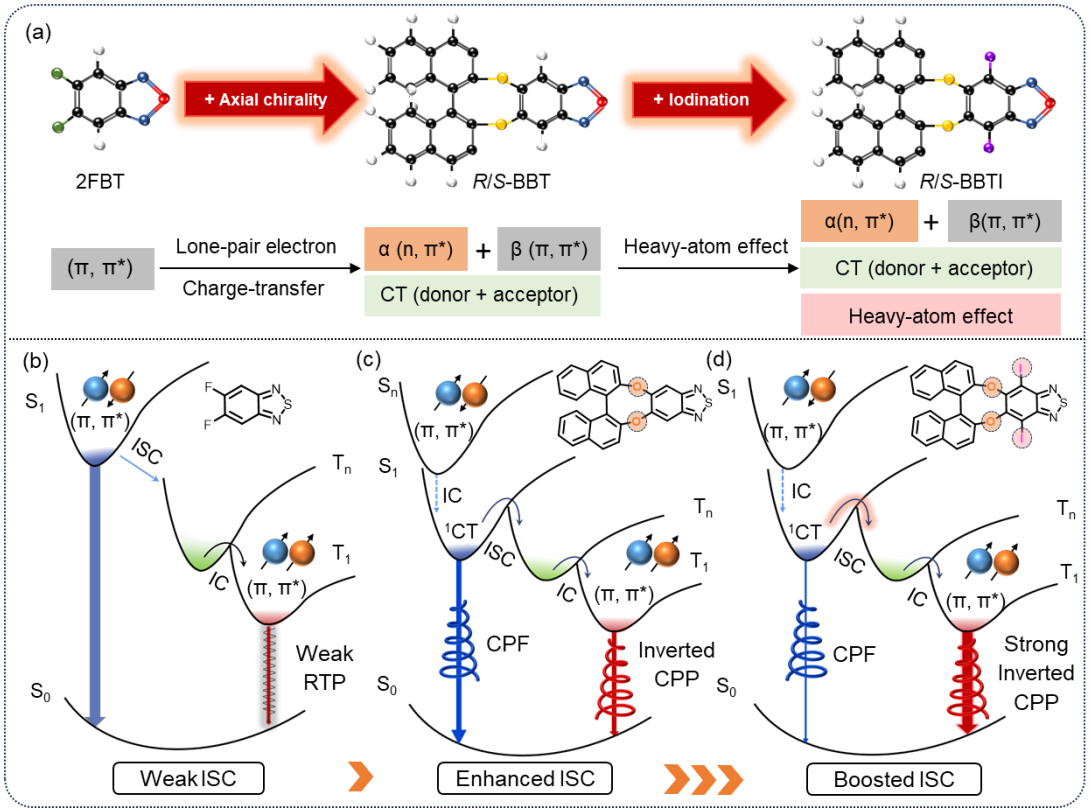

Figure 1. (a) Molecular design strategy of efficient CPP materials. Proposed mechanism of CPP using Jablonski diagram, (b) **2FBT** exhibits poor intersystem crossing (ISC), resulting in weak phosphorescence, (c) *R*/*S*-**BBT** showing enhanced ISC after incorporating lone-pair electron and charge transfer character leads to circularly polarized fluorescence (CPF) and moderate inverted CPP, (d) *R*/*S*-**BBTI** showing strong inverted CPP owing to the synergistic contributions of lone-pair electron, charge-transfer, and heavy-atom effect.

The commercially available 5,6-difluorobenzo[c][1,2,5]thiadiazole (**2FBT**) was

purified by column chromatography followed by recrystallization from toluene three times before use. *R*/*S*-**BBT** and *R*/*S*-**BBTI** were synthesized by one-step condensation of enantiomerically pure (*R*/*S*)-(+/-)-1,1′-bi(2-naphthol) with **2FBT** and 5,6-difluoro-4,7-diiodobenzo[c][1,2,5]thiadiazole, respectively. *R*/*S*-**BBT** and *R*/*S*-**BBTI** were purified by column chromatography and multiple recrystallizations. All compounds were fully characterized by ^{1}H NMR, ^{13}C NMR, high-resolution mass spectrometry (HRMS), and high-performance liquid chromatography (HPLC) to ensure their high purity (supplementary Fig. S1-S17). The crystal data of **2FBT** was obtained from the Cambridge Crystallographic Data Centre (CCDC number: 1862923).[30] The *R*-**BBT** and *R*/*S*-**BBTI** crystals were successfully grown by solvent evaporation and analyzed by X-ray crystallography (Fig. 2a, Fig. S18-S23, and Table S1). In contrast to the **2FBT** single crystal, neither *R*-**BBT** nor *R*/*S*-**BBTI** exhibited strong π-π interactions in their crystal packings, examining their packing only F···H, N···S, N···N, S···H, O···H and F···F exist due to the highly twisted helical structures (Figure 2a). These interactions work together to suppress molecular motion in the crystal enhancing phosphorescence efficiency. This was due to the highly twisted helical structures of *R*-**BBT** and *R*/*S*-**BBTI**. The *R*-**BBTI** and *S*-**BBTI** enantiomers packed in a chiral orthorhombic space group of P21 with the flack parameters of -0.0063 and 0.0320 confirmed their absolute axial chiral structures.

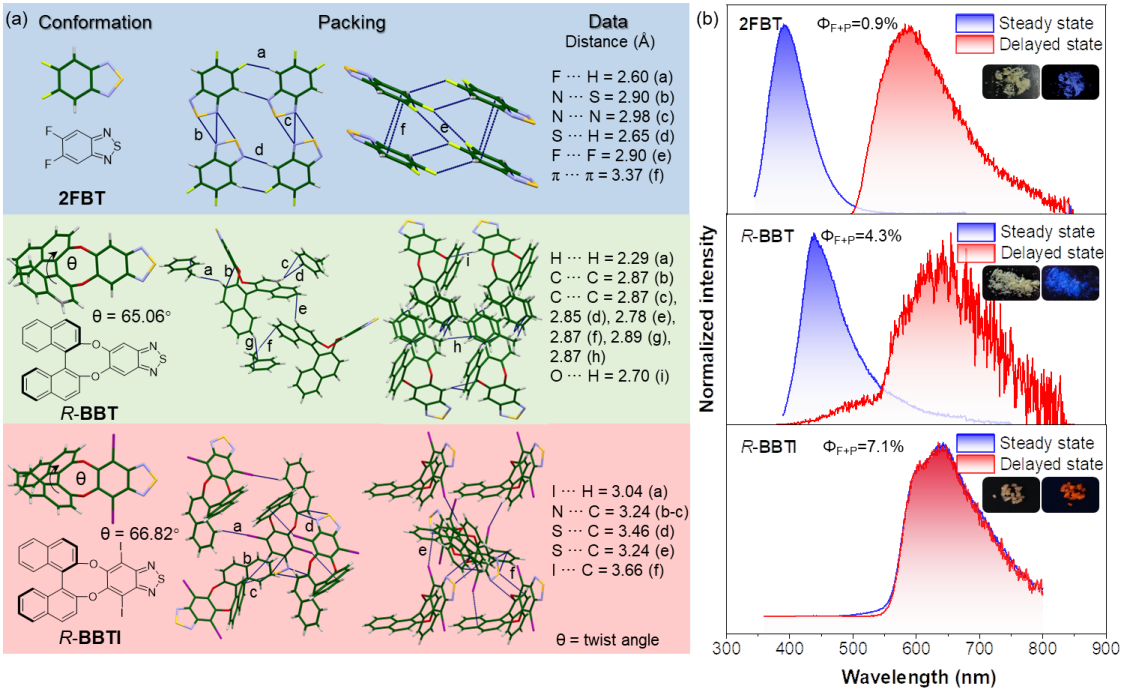

Figure 2. (a) Single-crystal X-ray diffraction (SC-XRD) crystallographic packing units and structures of **2FBT**, *R*-**BBT**, and *R*-**BBTI**; (b) Normalized photoluminescence spectra of **2FBT**, *R*-**BBT**, and *R*-**BBTI** crystals in steady state (blue shallow) and delayed states after 1 ms (red shallow), Inset: the corresponding photographs of the crystals under daylight (Left) and 365 nm UV light excitation (Right).

Normally, organic RTP phenomena rely heavily on the restriction of molecular motion in the crystalline state or doped solid film.[4] Therefore, detailed photophysical studies

of **2FBT**, *R*/*S*-**BBT**, and *R*/*S*-**BBTI** were initially performed in their crystalline states (Fig. 2b and Figure S24). The steady-state PL spectra of **2FBT** and *R*/*S*-**BBT** crystals showed blue emission at 392 and 440 nm, respectively, while their delayed-state PL spectra after 1 ms exhibited red to NIR emission at 587 and 640 nm. For *R*/*S*-**BBTI** crystals, both steady-state and delayed-state spectra showed a dominant NIR emission band at approximately 650 nm, redshifted compared to the delayed peaks of **2FBT** and *R*/*S*-**BBT** due to increasing conjugation, donor-acceptor (D-A) nature, and heavy atomic effect. The emission lifetime measurements further confirmed the spin states of these two peaks. The lifetimes at short wavelengths were 0.6, 0.7, and 1.0 ns for **2FBT**, *R*-**BBT**, and *R*-**BBTI**, respectively. In contrast, their lifetimes at longer wavelengths were measured as 216, 65, and 163 μs under ambient conditions (Fig. S25). Therefore, the blue emission can be assigned as fluorescence, while the peaks at longer wavelengths are phosphorescence. In addition, the total photoluminescent quantum yields (PLQY) gradually increased from 0.9% (**2FBT**) to 4.3% (*R*-**BBT**) and 7.0% (*R*-**BBTI**). The ISC rates also improved from 3.3×10^6 (**2FBT**) to 4.3×10^6 (*R*-**BBT**) and 7.0×10^6 (*R*-**BBTI**) (Table S2).

Dual emission peaks at ~450 nm and ~640 nm were observed for dilute solutions of *R*/*S*-**BBTI** across various solvents (Fig. 3a). The NIR emission at 640 nm matched with the phosphorescence peak in the solid state, indicating that *R*/*S*-**BBTI** may exhibit phosphorescence even in dilute solution. To verify the nature of 640 nm emission, PL spectra of *R*/*S*-**BBTI** were measured in toluene and *N*, *N*-dimethylformamide (DMF) before and after deoxygenation (Fig. 3b and Fig. S26). The significant enhancement of the NIR emission after deoxygenation demonstrated that *R*/*S*-**BBTI** were oxygen-sensitive probes and the 640 nm band was phosphorescence. Additional PL measurements in different water and THF mixtures revealed that PL enhancement of the 640 nm band at 90% water fraction was attributable to aggregation, where RIM played a crucial role. Moreover, the formation of these aggregates prevented the quenching of the triplet state by oxygen, leading to an overall increase in PL (Fig. S27-S28). In the aggregates, the PL enhancement was the synergistic effect of RIM and prevention from oxygen quenching in the aggregate emission. Furthermore, temperature-dependent PL spectra revealed that the emission intensity at 640 nm gradually decreased with increasing temperature, providing additional evidence for the phosphorescent nature of the 640 nm band (Fig 3c). The emission lifetimes of *R*/*S*-**BBTI** at 650 nm in tetrahydrofuran (THF) solution decreased from 477 μs (80 K) to 38 μs (300 K) (Fig. 3c and Fig. S29). Together, these systematic experimental results provided unambiguous evidence for the remarkable RTP phenomenon of *R*/*S*-**BBTI** in solution. The current observation of solution NIR phosphorescence is rare and can be attributed to the molecular design and enhanced spin-orbit coupling, which facilitates ISC and enables phosphorescence in solution.

With axial chirality, the chiroptical properties of the enantiomerically pure *R*/*S*-**BBT** and *R*/*S*-**BBTI** were investigated by circular dichroism (CD) and CPL spectra in solution states. The CD spectra of enantiomers exhibited good mirror images with

alternating positive and negative Cotton effects from 200 to 500 nm (Fig. 3d). Obvious mirror-imaged CPL profiles of *R*/*S*-**BBTI** were observed in THF solutions (Fig. 3e). Excitingly, the CPL spectra of *R*/*S*-**BBTI** showed not only blue emission but also long-wavelength NIR emission at 640 nm. The corresponding g_{lum} at emission maxima reached ±0.007 in the THF solution. Similar dual emissions were achieved in the toluene solution. In Fig. 3f, the NIR emission at 640 nm in toluene was significantly enhanced after deoxygenation, verifying its phosphorescence nature. Notably, the CPP demonstrated an inverted CPL signal and amplified intensity approximately 2-3 times higher than circularly polarized fluorescence at the same condition. It is worth mentioning that this is a breakthrough since all previous reports of CPP phenomena are achieved in aggregate or doped solid states.[18]

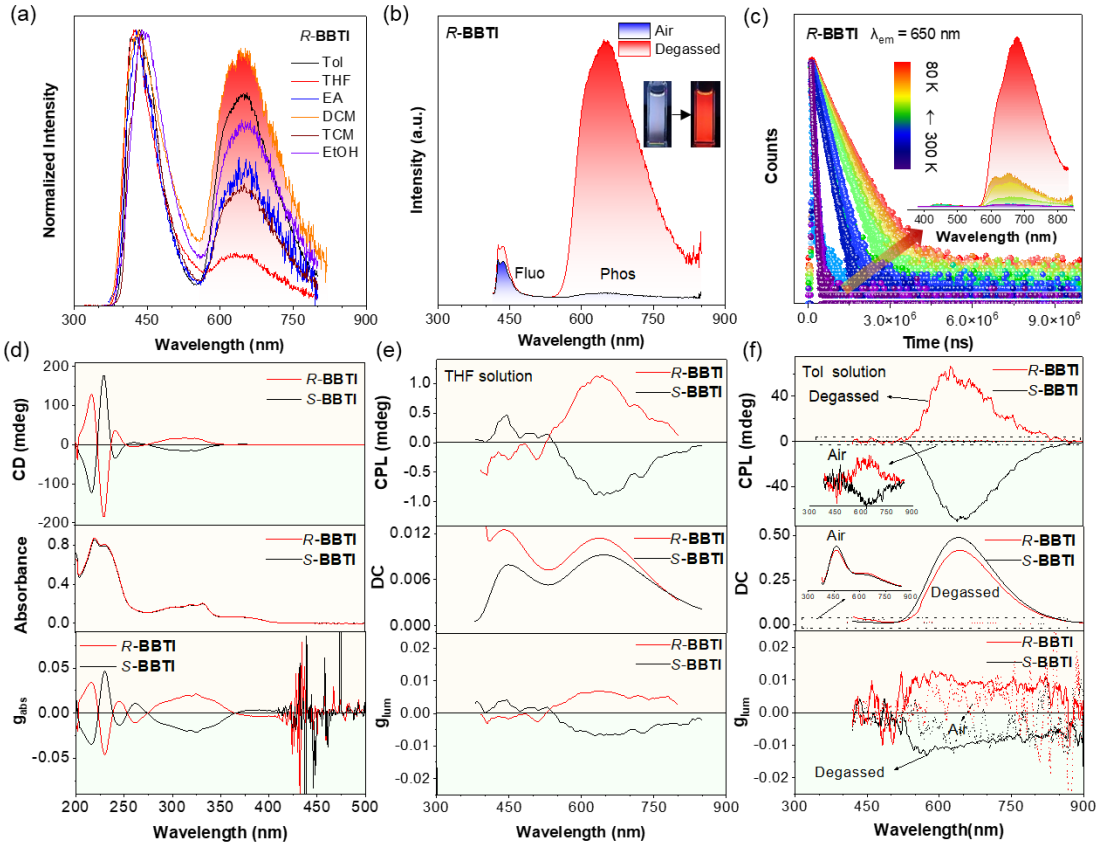

Figure 3. Photophysical properties of *R*/*S*-**BBTI** in solution (a) PL spectra of *R*-**BBTI** in toluene, THF, ethyl acetate (EA), dichloromethane (DCM), trichloromethane (TCM), and ethyl alcohol (EtOH) solution; (b) PL spectra of *R*-**BBTI** in toluene before and after deoxygenation; (c) PL spectra and PL decay curves of *R*-**BBTI** at different temperatures from 77 K to 298 K in THF solution; (d) CD and UV−vis spectra of *R*/*S*-**BBTI** in acetonitrile solution; (e) CPL spectra, direct current (DC) spectra and the dissymmetry factors of *R*/*S*-**BBTI** in THF solution; (f) CPL spectra, DC spectra and the dissymmetry factors of *R*/*S*-**BBTI** in toluene solution before and after deoxygenation [Concentration: 10^{-5} M].

Theoretical calculations were carried out to understand the abnormal NIR-CPP in the solution.[31] As depicted in Fig. 4a and Fig. S30, **2FBT** showed locally excited (LE)

characters in both excited singlet (S_1) and triplet (T_1) states. However, *R*/*S*-**BBT** and *R*/*S*-**BBTI** with highly twisted D-A structures exhibited CT characters in S_1 states and LE characters in T_1 states, accompanied by decreased excited singlet and triplet state energy levels. The Multiwfn program was used for quantifying the compositions of π and non-bonding orbitals (n orbital).[32, 33] Compared to **2FBT** and *R*/*S*-**BBT**, *R*/*S*-**BBTI** has greater n orbital contributions of 35.4% in the S_1 state, thus enabling efficient SOC from ^{1}(n–π*) to ^{3}(π–π*) according to El-Sayed's rule. The ORCA program at the DKH-def2-TZVP basis set further calculated the SOC constants of these compounds.[34] SOC efficiency could be improved by incorporating lone-pair electrons and increasing heavy atomic nuclear charge (Fig. S31). For *R*-**BBTI**, the SOC value $\xi(S_0, T_1)$ was calculated as 5.55 cm^{-1} and $\xi(S_1, T_1)$ as 61.48 cm^{-1}. Such highly efficient SOC would tremendously enhance the ISC efficiency and formation of triplet excitons by the spin-flip process.

Besides the ISC, the non-radiative process also significantly impacts the NIR phosphorescence efficiency. To investigate changes in molecular configuration during the excitation process, reorganization energy and root-mean-square deviation (RMSD) values were calculated (Fig. 4b and Figure S32-40).[32] The ground-state (blue) and excited-state (red) geometries of *R*/*S*-**BBTI** were nearly identical in the gas phase, with small RMSD values of 0.119 Å (S_0 *vs* S_1) and 0.039 Å (S_0 *vs* T_1).[35] Using the ONIOM model, the excitation process was analyzed in the crystal, revealing slightly reduced RMSD values of 0.078 Å (S_0 *vs* S_1) and 0.033 Å (S_0 *vs* T_1) with the perfect geometrical overlap.[36] These calculation results suggest the molecular configurations in the two states have differing rigidity, with crystals being more rigid than gaseous molecules and having varying degrees of restriction in their intramolecular motions. Similar total reorganization energy (λ) values in the gas and crystalline phases also quantitatively supported the above results.[37] Furthermore, λ was mainly contributed by the changes in the high-frequency region. The bond length contribution exceeded 87%, but the dihedral angle hardly changed, indicating the primary motion mode is the stretching vibration of the aromatic ring. Therefore, the molecular structures are highly rigidified by ring-locked engineering to suppress the non-radiative process of triplet excitons.

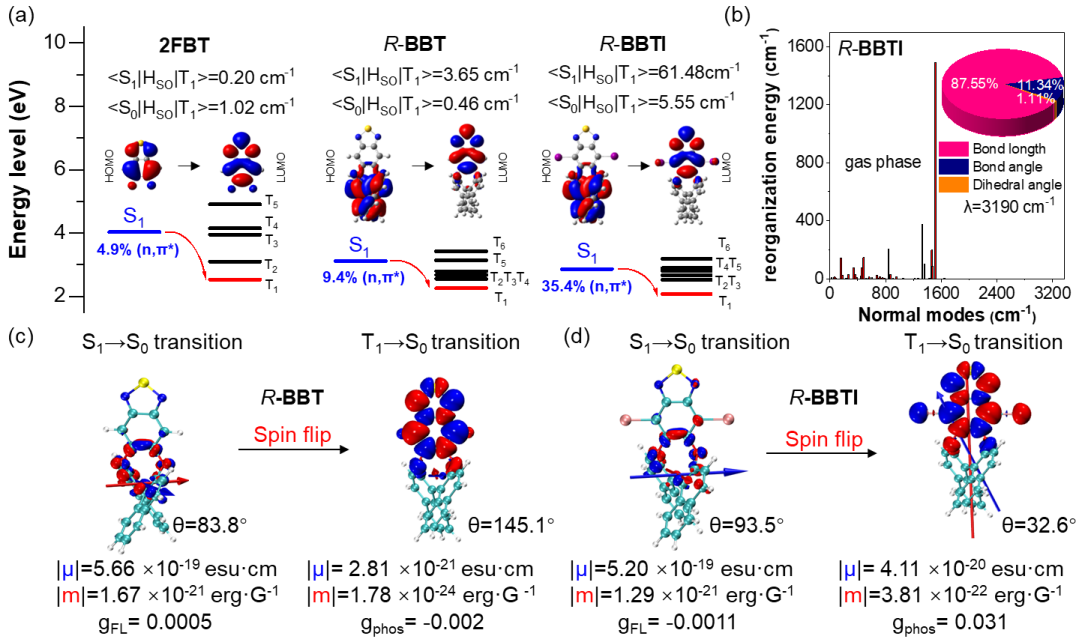

Figure 4. (a) The calculated energy levels, electron cloud distribution, composition of n-π* transition, and spin-orbit coupling constant. (b) Plots of reorganization energy versus normal mode wavenumber of *R*-**BBTI** in the gas phase calculated by TD-DFT method. Inset: Proportions of bond length, bond angle, and dihedral angle contributed to the total reorganization energy. (c, d) The orientation and magnitude of μ (blue stick) and *m* (blue stick) vectors for *R*-**BBT** (c) and *R*-**BBTI** (d) in the $S_1 \rightarrow S_0$ and $T_1 \rightarrow S_0$ transitions.

To elucidate the mechanism of NIR-CPP and its key influencing factors, we calculated the transition density and the transition magnetic (*m*) and electronic dipole moments (μ) for the S_1-S_0 and T_1-S_0 transitions (Fig. 4c-d and Fig. S41).[31, 38] Owing to the highly twisted helical molecular structure, *m* and μ were oriented perpendicular in the S_1-S_0 transition for *R*/*S*-**BBT** and *R*/*S*-**BBTI**. As a result, circularly polarized fluorescence emission is nearly negligible. However, due to the electron spin-flip and orbital angular momentum changes during the ISC process, the orientations of *m* and μ altered dramatically. Meanwhile, *m* was significantly enhanced by 200 times under the heavy-atom effect compared to that of *R*/*S*-**BBT** in the T_1-S_0 transition. The changed orientation and increased magnitude of *m* explain the high experimental value of g_{phos} for *R*/*S*-**BBTI**. The calculated chiroptical properties of the two enantiomers were summarized in Table S3. Notably, the transition density provides a more intuitive understanding of the difference between μ and *m*. For the S_1-S_0 transition, minimal overlap of transition orbital occurs only near the highly torsional eight-membered ring. *R*/*S*-**BBTI** exhibited a radiative charge transfer process from binaphthalene to benzothiadiazole units for the S_1-S_0 transition. In contrast, extensive transition density was localized on the benzothiadiazole unit for the T_1-S_0 transition, enabling significant transition dipole moments. These results demonstrate the role of spin-flip in regulating the orientation and magnitude of transition dipole moments for triplet states, which significantly impacts CPP emission. The extended delocalization and highly twisted

rigid structure enable high-performance CPP emitters.

Surprisingly, *R*/*S*-**BBTI** in the as-prepared dimethyl sulfoxide (DMSO) solution exhibited only blue emission initially, but NIR phosphorescence was quickly activated upon UV irradiation (Fig. S42-43). A dilute DMSO solution (10^{-5} mol/L) of *S*-**BBTI** was irradiated from the bottom with a 365 nm UV light (optical power density ca. 1.5 W cm^{-2}). Intense NIR emission emerged from the bottom and diffused within 10 s (Fig. 5a-b). The PLQY increased from 0.3% to 4.2% during UV irradiation. The original blue emission was restored by shaking the solution vial. Similar photoactivation and oxygen-quenching occur in some gold and copper complexes, inspiring mechanistic elucidation.[39, 40] After 2 h UV irradiation of dilute *S*-**BBTI** in DMSO-d_6, a new ^{1}H NMR peak at 3.05 ppm was observed, assigned to methylsulfonylmethane (MSM) (Fig. 5c). Furthermore, the absorption spectra before and after UV light irradiation remained almost unchanged, demonstrating that *S*-**BBTI** was stable and did not transform into new compounds (Fig. S44). The CD and CPL spectra of *R*/*S*-**BBTI** in DMSO were also monitored before and after UV irradiation. In contrast, the CD spectra were nearly unchanged after UV irradiation for 10 s (Fig. S45), and obvious photoactivated mirror-image CPL profiles were observed (Fig. 5d). Although *R*/*S*-**BBT** solutions did not exhibit such photoactivated CPP phenomena, their PMMA films showed obvious CPP emission under UV irradiation (Fig. S46-S49). Remarkably, the g_{phos} values of *R*/*S*-**BBTI** reached +0.012 and -0.013, respectively.

To further investigate the detailed mechanism of photoactivation, some commercial reactive oxygen species (ROS) indicators were used to identify the types of ROS generated (Fig. S50).[41, 42] Dichlorodihydrofluorescein diacetate (DCFH-DA) for all ROS detection, dihydrorhodamine 123 (DHR123) for $O_2^{-\bullet}$ detection, and hydroxyphenyl Fluorescein (HPF) for •OH detection all showed significantly increased luminescence intensity upon UV light irradiation of *R*/*S*-**BBT** and *R*/*S*-**BBTI** at different times. However, the absorbance of 9,10-anthracenediyl-bis(methylene)dimalonic acid (ABDA), an indicator for singlet oxygen ($^1O_2$) detection, remained nearly unchanged. More convincingly, electron spin resonance (ESR) spectra showed that the formation of 5,5-dimethyl-1-pyrroline *N*-oxide (DMPO) radical adducts DMPO-OH and DMPO-OO were formed in the *S*-**BBTI** system, confirming the presence of $O_2^{-\bullet}$ and •OH species, but the absence of $^1O_2$ in the *R*/*S*-**BBTI** DMSO solution upon UV light irradiation (Figure 5e and Fig. S51). Therefore, these results demonstrate that CPP materials generate ROS through the type I mechanism involving $O_2^{-\bullet}$ and •OH. Subsequently, the DMSO solution reacted and produced MSM, gradually creating a local hypoxic microenvironment that activated the phosphorescence.

The photoactivated properties and high compatibility of these CPP materials were further demonstrated through anti-counterfeiting in solution, gel, and film states (Fig. S52-53, Movie S1). Tetradecyl ammonium malonate was selected as the initiator to gelatinate DMSO to slow down the oxygen diffusion.[43] The photoactivation of a cat-paw pattern in the gel surface was achieved by UV irradiating, while the erasing process

was accomplished by liquefying the gel heating. In the doped-PMMA film with 0.5 mm thickness, the information could be written by UV light and erased in the dark after about 4 h.

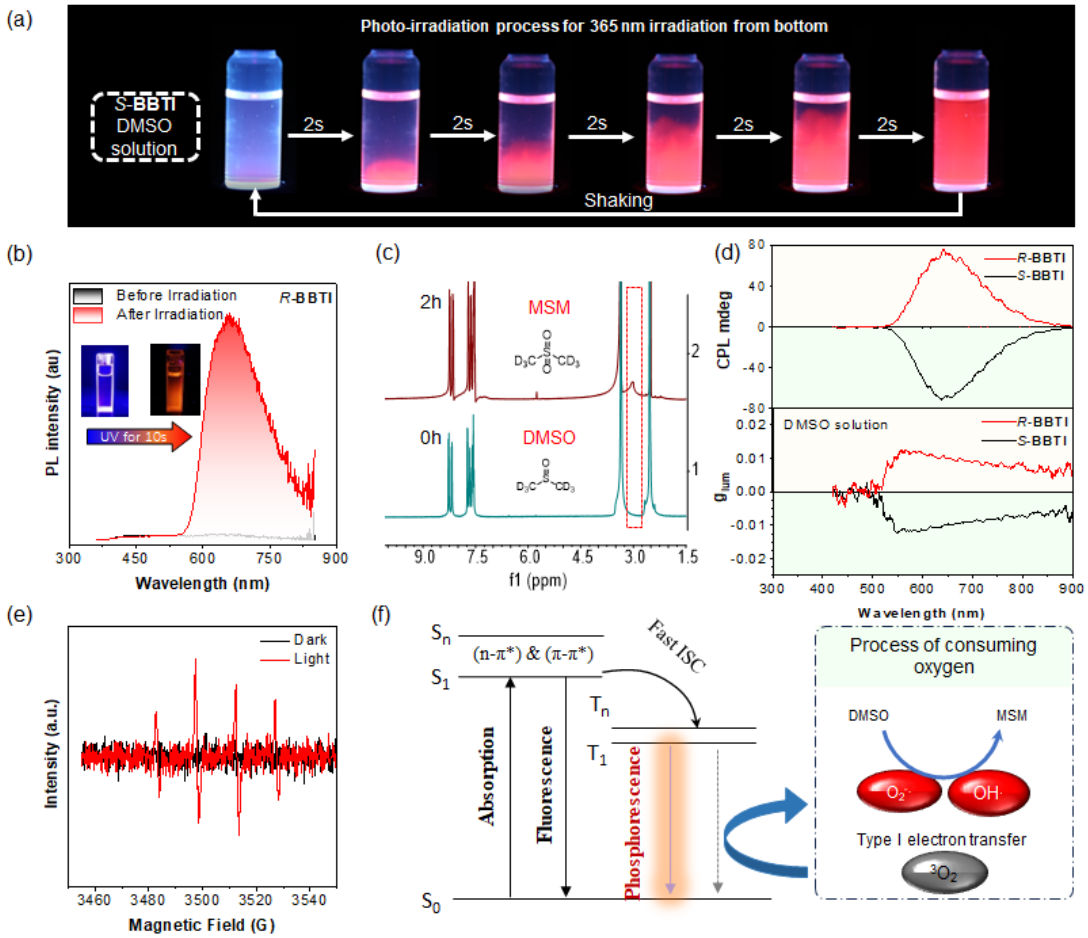

Figure 5. Photophysical properties of *R/S*-**BBTI** in DMSO solution (10^{-5} M). (a) Snapshots of an aerated DMSO solution of *S*-**BBTI** in a quartz cuvette upon irradiation from the bottom with a 365 nm UV flashlight at 298 K; (b) The photoluminescence spectra of *R*-**BBTI** in DMSO solution before and after UV irradiation; (c) ^{1}H NMR traces of an aerated DMSO solution of *S*-**BBTI** after 0 and 2 hours irradiation at 298 K using a 365 nm UV lamp (optical power density ca. 1.5 W/cm^2); (d) CPL spectra and g_{lum} value of *R/S*-**BBTI** in DMSO solution before and after UV irradiation; (e) DMPO radical adducts DMPO-OH formed in the *R*-**BBTI** system in ultrapure water; (f) Photo activated CPP mechanism of *R/S*-**BBTI** in DMSO solution.

Inspired by the superior oxygen-sensitive properties, *R/S*-**BBTI** was anticipated to be a highly promising material for hypoxia bioimaging. Hela cells were incubated with *S*-**BBTI** and imaged with the confocal microscope under varying oxygen levels (Table S4). As expected, the stained cells exhibited negligible phosphorescence in the air. However, obvious increases in phosphorescence were observed when the Hela cells were incubated in a hypoxic condition (2% O_2). Significant photoactivated phosphorescence was observed after the UV light irradiation (Fig. 6a). Furthermore, *S*-**BBTI** nanoparticles with DSPE-PEG (2000) were fabricated by a bottom-up approach,

and the Hela cells xenograft mice model was constructed and treated with *S*-**BBTI** nanoparticles by intravenous injection at the specified time intervals (Fig. 6b-f). The tumor and other organs were then collected in an anaerobic glove box and imaged with 390 nm excitation. The results in Fig. 5e showed intensive phosphorescence in the isolated hypoxia tumors up to 72 h, probably due to the enhanced permeability and retention (EPR) effect.[44] In addition, the phosphorescence intensity indicated heterogeneous oxygen distribution in the tumor with much stronger phosphorescence in the core than in the periphery areas, suggesting more hypoxia centrally. Partial nanoparticle distribution in mice organs, such as the liver and lung, was observed 12 h after administration. However, no significant phosphorescence was detectable 24 hours later, potentially attributable to the EPR effects. These results demonstrated that *S*-**BBTI** could visualize the hypoxia region of tumors *in vivo*.

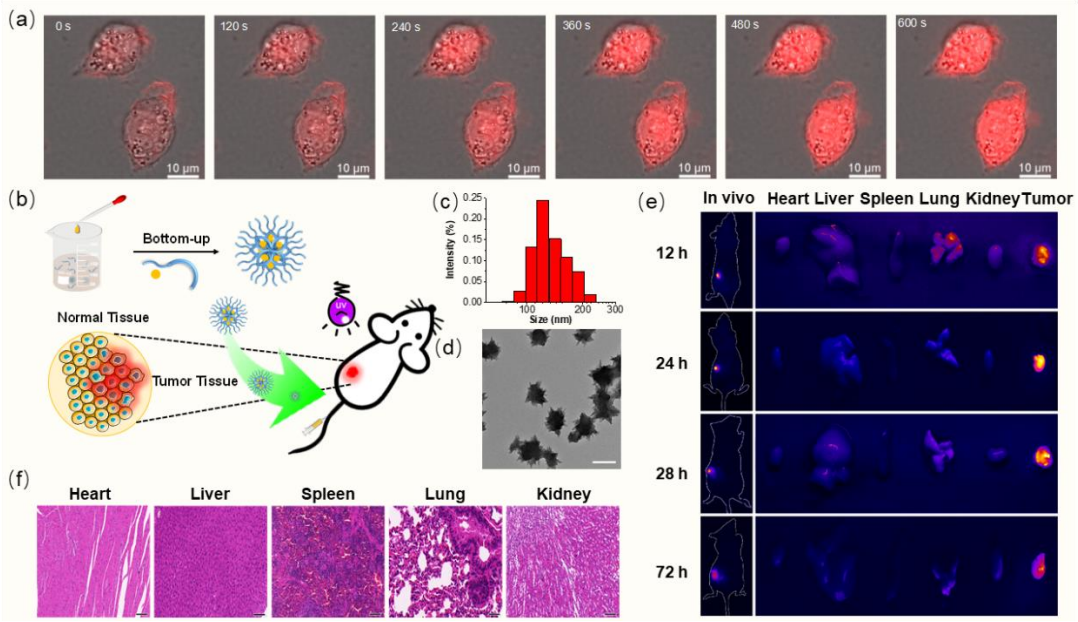

Figure 6. *In vitro* and *in vivo* oxygen-sensitive phosphorescent imaging application. (a) Hela cells were treated with *S*-**BBTI** (20 μM) for 12 h in hypoxia and visualized by confocal image after laser irradiation (390 nm); (b) A bottom-up approach to synthesize the water-soluble nanoparticles of *S*-**BBTI** and DSPE-PEG (2000), then the aqueous solution was injected into Hela cells xenograft mice model. (c,d) DLS and TEM images (inset) of *S*-**BBTI**-based NPs. The scale bar in TEM images is 100 nm; (e) Hypoxia imaging in living and tissue: vivo imaging of Hela cells xenograft mice model and separated organs after intravenous injection at the indicated time scales (390 nm). (f) Immunohistochemical analysis of hematoxylin-eosin staining in organs from mice with treatments of *S*-**BBTI** (10 mg/kg) for 72 h. The scale bar in TEM images is 100 μm.

In summary, a facile strategy to realize NIR-CPP emitters with spiral ring-locked heteroaromatic systems is reported. The heavy-atom effect, CT characteristics, and rigid twist heterocyclic configuration play crucial roles in obtaining efficient NIR-CPP in both solution and aggregate states. The heavy iodine atoms facilitate the ISC process and improve the phosphorescence efficiency. Meanwhile, the rigid twist heterocyclic configuration suppresses non-radiative transitions and accelerates the phosphorescence

decay. Based on this design principle, a series of enantiomers featuring photoactivated NIR-CPP are obtained via efficient synthetic routes, demonstrating the potential of materials of different shapes for information encryption and hypoxia imaging in cells and tumors. Our investigation highlights the importance of the spin-flip process and the orientation of the transition electric and magnetic dipole moments, significantly improving CPP efficiencies. Our findings reveal the photoactivated phosphorescence and CPP mechanism of small organic molecules and offer new opportunities for expanding the applicability for diversified applications.

Online content

Any methods, additional references, Nature Research reporting summaries, source data, extended data, supplementary information, and statements of data and code availability are available at ···

Acknowledgments

We thank the Materials Characterization and Preparation Center, The Chinese University of Hong Kong, Shenzhen, for materials characterization, and we are grateful to Xuan Li for her help with high-resolution mass measurements. This work was supported by the National Natural Science Foundation of China grant (52273197, 52333007, 52250410355, and 52303382); the Shenzhen Key Laboratory of Functional Aggregate Materials (ZDSYS 20211021111400001); the Science, Technology, and Innovation Commission of Shenzhen Municipality (JCYJ 2021324134613038, JCYJ20220530143805012, KQTD 20210811090142053, GJHZ 20210705141810031, JCYJ20220818103007014, and RCBS20221008093130084); the Innovation and Technology Commission (ITCCNERC14SC01); Science and Technology Program of Guangzhou, China (2023A04J0069).

Author contributions

Z.Q., Z.Z., and B.Z.T. supervised the project. D. L. designed and synthesized the molecules, carried out the measurements of the photophysical characteristics. W. W. performed the cell and animal experiments. D. L. and Z. Y. performed theoretical calculations. K. W., L. Z., Y. X., S. C., B. W., and Q. W. contributed to discussions. D. L., P. A., Z. Q., and Z. Z. contributed to the manuscript writing. All authors discussed the progress of the research and reviewed the manuscript.

Competing financial interests

The authors declare no competing financial interests.

Received: …;
Accepted: …;
Published online: …

References

1. Ye WP*, et al.* Confining isolated chromophores for highly efficient blue phosphorescence. *Nat Mater* **20**, 1539-1544 (2021).

2. Chen C*, et al.* Carbazole isomers induce ultralong organic phosphorescence. *Nat Mater* **20**, 175-180 (2021).

3. Chanmungkalakul S*, et al.* A Descriptor for Accurate Predictions of Host Molecules Enabling Ultralong Room-Temperature Phosphorescence in Guest Emitters. *Angew Chem, Int Ed* **61**, e202200546 (2022).

4. Zhao W, He Z, Tang BZ. Room-temperature phosphorescence from organic aggregates. *Nat Rev Mater* **5**, 869-885 (2020).

5. Cai SZ, Yao XK, Ma HL, Shi HF, An ZF. Manipulating intermolecular interactions for ultralong organic phosphorescence. *Aggregate* **4**, e320, (321-319) (2023).

6. Kabe R, Notsuka N, Yoshida K, Adachi C. Afterglow Organic Light-Emitting Diode. *Adv Mater* **28**, 655-660 (2016).

7. Miao Q*, et al.* Molecular afterglow imaging with bright, biodegradable polymer nanoparticles. *Nat Biotechnol* **35**, 1102-1110 (2017).

8. Yu X, Zhang H, Yu J. Luminescence anti-counterfeiting: From elementary to advanced. *Aggregate* **2**, 20-34 (2021).

9. Dang Q*, et al.* Room-Temperature Phosphorescence Resonance Energy Transfer for Construction of Near-Infrared Afterglow Imaging Agents. *Adv Mater* **32**, 2006752 (2020).

10. Hirata S, Vacha M. Circularly Polarized Persistent Room-Temperature Phosphorescence from Metal-Free Chiral Aromatics in Air. *J Phys Chem Lett* **7**, 1539-1545 (2016).

11. Huang Z, He Z, Ding B, Tian H, Ma X. Photoprogrammable circularly polarized phosphorescence switching of chiral helical polyacetylene thin films. *Nat Commun* **13**, 7841 (2022).

12. Li H*, et al.* Single-component color-tunable circularly polarized organic afterglow through chiral clusterization. *Nat Commun* **13**, 429 (2022).

13. Gu L*, et al.* Circularly polarized organic room temperature phosphorescence from amorphous copolymers. *J Am Chem Soc* **143**, 18527-18535 (2021).

14. Chen W, Tian Z, Li Y, Jiang Y, Liu M, Duan P. Long-Persistent Circularly Polarized Phosphorescence from Chiral Organic Ionic Crystals. *Chem Eur J* **24**, 17444-17448 (2018).

15. Liang X*, et al.* Organic Room-Temperature Phosphorescence with Strong Circularly Polarized Luminescence Based on Paracyclophanes. *Angew Chem, Int Ed* **58**, 17220-17225 (2019).

16. Zhang D-W, Li M, Chen C-F. Axially chiral materials exhibiting blue-emissive ultralong organic phosphorescence and intense circularly polarized luminescence.

Sci China Mater **66**, 4030-4036 (2023).

17. He T, Guo W-J, Chen Y-Z, Yang X-F, Tung C-H, Wu L-Z. Ratiometric hypoxia detection by bright organic room temperature phosphorescence of uniformed silica nanoparticles in water. *Aggregate* **4**, e250 (2023).

18. Wang XJ, Ma S, Zhao B, Deng JP. Frontiers in Circularly Polarized Phosphorescent Materials. *Adv Funct Mater* **33**, 2214364 (2023).

19. Sun H, Zhu L. Achieving purely organic room temperature phosphorescence in aqueous solution. *Aggregate* **4**, e253 (2023).

20. Khan A*, et al.* Intramolecular-Locked High-Efficiency Ultrapure Violet-Blue (CIE-y <0.046) Thermally Activated Delayed Fluorescence Emitters Exhibiting Amplified Spontaneous Emission. *Adv Funct Mater* **31**, 2009488 (2021).

21. Xiong JB*, et al.* Evidence for Aggregation-Induced Emission from Free Rotation Restriction of Double Bond at Excited State. *Org Lett* **20**, 373-376 (2018).

22. Aizawa N*, et al.* Delayed fluorescence from inverted singlet and triplet excited states. *Nature* **609**, 502-506 (2022).

23. Yuan YX*, et al.* Enhanced DNA Sensing and Chiroptical Performance by Restriction of Double-Bond Rotation of AIE cis-Tetraphenylethylene Macrocycle Diammoniums. *Org Lett* **22**, 1836-1840 (2020).

24. Luo X-F, Song S-Q, Wu X, Yip C-F, Cai S, Zheng Y-X. A chiral spirofluorene-embedded multiple-resonance thermally activated delayed fluorescence emitter for efficient pure-green circularly polarized electroluminescence. *Aggregate*, e445 (2023).

25. Kato K*, et al.* Circularly polarized luminescence from a common alkoxy pillar[5]arene and its co-aggregates with π-conjugated rods. *Aggregate*, e482 (2024).

26. Xiong J-B*, et al.* The Fixed Propeller-Like Conformation of Tetraphenylethylene that Reveals Aggregation-Induced Emission Effect, Chiral Recognition, and Enhanced Chiroptical Property. *J Am Chem Soc* **138**, 11469-11472 (2016).

27. Peng Q, Ma HL, Shuai ZG. Theory of Long-Lived Room-Temperature Phosphorescence in Organic Aggregates. *Accounts Chem Res* **54**, 940-949 (2021).

28. Yang Z*, et al.* Boosting the Quantum Efficiency of Ultralong Organic Phosphorescence up to 52 % via Intramolecular Halogen Bonding. *Angew Chem*

Inter Ed **59**, 17451-17455 (2020).

29. Sun SY, Ma LW, Wang J, Ma X, Tian H. Red-light excited efficient metal-free near-infrared room-temperature phosphorescent films. *Natl Sci Rev* **9**, nwab085 (2022).

30. Ams MR, Trapp N, Schwab A, Milic JV, Diederich F. Chalcogen Bonding "2S-2N Squares" versus Competing Interactions: Exploring the Recognition Properties of Sulfur. *Chemistry* **25**, 323-333 (2019).

31. Frisch MJ*, et al.* Gaussian 16 Rev. C.01. Wallingford CT (2016).

32. Lu T, Chen F. Multiwfn: a multifunctional wavefunction analyzer. *J Comput Chem* **33**, 580-592 (2012).

33. Lu T, Chen Q. A simple method of identifying π orbitals for non-planar systems and a protocol of studying π electronic structure. *Theor Chem Acc* **139**, 25 (2020).

34. Neese F. Software update: the ORCA program system, version 4.0. *WIREs Comput Mol Sci* **8**, e1327 (2017).

35. William Humphrey AD, and Klaus Schulten. VMD: Visual Molecular Dynamics. *J Mol Graph*, 33-38 (1996).

36. Zhang K*, et al.* Novel Deep Red Thermally Activated Delayed Fluorescence Molecule with Aggregation-Induced Emission Enhancement: Theoretical Design and Experimental Validation. *J Phys Chem Lett* **13**, 4711-4720 (2022).

37. Shuai Z. Thermal Vibration Correlation Function Formalism for Molecular Excited State Decay Rates. *Chin J Chem* **38**, 1223-1232 (2020).

38. Aidas K*, et al.* The Dalton quantum chemistry program system. *Wiley Interdiscip Rev Comput Mol Sci* **4**, 269-284 (2014).

39. Wan S, Lu W. Reversible Photoactivated Phosphorescence of Gold(I) Arylethynyl Complexes in Aerated DMSO Solutions and Gels. *Angew Chem, Int Ed* **56**, 1784-1788 (2017).

40. Jin Y*, et al.* Aggregation-induced barrier to oxygen-a new AIE mechanism for metal clusters with phosphorescence. *Natl Sci Rev* **9**, nwab216 (211-219) (2022).

41. Gomes A, Fernandes E, Lima JL. Fluorescence probes used for detection of reactive oxygen species. *J Biochem Biophys Methods* **65**, 45-80 (2005).

42. Feng GX, Zhang GQ, Ding D. Design of superior phototheranostic agents guided by Jablonski diagrams. *Chem Soc Rev* **49**, 8179-8234 (2020).

43. Sahoo P, Adarsh NN, Chacko GE, Raghavan SR, Puranik VG, Dastidar P. Combinatorial library of primaryalkylammonium dicarboxylate gelators: a supramolecular synthon approach. *Langmuir* **25**, 8742-8750 (2009).

44. Nichols JW, Bae YH. EPR: Evidence and fallacy. *J Control Release* **190**, 451-464 (2014).